published by Ural Federal University
eISSN 2411-1414
chimicatechnoacta.ru

ARTICLE
2023, vol. 10(4), No. 202310414
DOI: 10.15826/chimtech.2023.10.4.14

Chemical stability aspects of $BaCe_{0.7–x}Fe_xZr_{0.2}Y_{0.1}O_{3–\delta}$ mixed ionic-electronic conductors as promising electrodes for protonic ceramic fuel cells

Liana Tarutina [ab*], Inna Starostina [ab], Gennady Vdovin [a],
Svetlana Pershina [a], Emma Vovkotrub [a], Anna Murashkina [c]

a: Institute of High-Temperature Electrochemistry, Ural Branch of the Russian Academy of Sciences, Ekaterinburg 620137, Russia
b: Laboratory of Hydrogen Energy, Ural Federal University, Ekaterinburg 620009, Russia
c: Saint Petersburg State University, Saint Petersburg 199034, Russia
* Corresponding author: hakimovaliana@rambler.ru

This paper belongs to a Regular Issue.

Abstract

Mixed ion-electron conductors (MIECs) are promising materials for air electrodes for protonic ceramic fuel cells (PCFCs) or oxygen permeation membranes. In this work, various aspects of the chemical stability of Co-free MIEC materials, $BaCe_{0.7–x}Fe_xZr_{0.2}Y_{0.1}O_{3–\delta}$, were studied, including their interaction with another functional material ($BaCe_{0.5}Zr_{0.3}Y_{0.1}Yb_{0.1}O_{3–\delta}$-based proton-conducting electrolyte) and gas components (H_2O, CO_2, and H_2). Chemical compatibility studies indicate no visible chemical interaction between the electrode and electrolyte materials even at 1200 °C, which is significantly higher than the operating temperatures (600–800 °C) of PCFCs. The treatments of $BaCe_{0.7–x}Fe_xZr_{0.2}Y_{0.1}O_{3–\delta}$ in different atmospheres at 1100 °C, according to the XRD, SEM, IR and Raman spectroscopy data, resulted in the formation of impurity phases. However, their extremely small amounts suggest that they may not form at the operating temperatures. Thus, it can be assumed that the studied materials can be good candidates for various electrochemical applications.

Keywords

mixed ion-electron conductors
protonic ceramic fuel cells
chemical stability
barium ferrite
chemical interaction
crystal structure

Received: 07.11.23
Revised: 04.12.23
Accepted: 04.12.23
Available online: 08.12.23

Key findings

- No phase transition in BCZYF0.6 at temperatures from 50 °C to 1000 °C was confirmed.
- Long-term co-annealing of powder mixtures BCZYFx and BCZYYb at 1200 °C allows predicting the relative stability of electrode and electrolyte phases.
- The investigated electrode materials have acceptable chemical stability in the atmosphere with high (70 vol.%) humidity, carbon dioxide, and hydrogen.

Supplementary materials

1. Introduction

The current problems related to environmental pollution and global warming have focused much attention on alternative energy sources. One of such sources is a solid oxide fuel cell (SOFC), a promising device for converting the chemical energy of fuels into electricity. SOFCs are attractive because of their environmental friendliness, energy efficiency, lack of noisy moving parts, and straightforward fuel selection [1–3]. A wide commercialization of SOFCs based on oxygen-ion electrolytes is limited by their high operating temperatures of 800–1000 °C, which lead to a rapid degradation of SOFC performance [4]. The use of protonic ceramic fuel cells (PCFCs) enables the operating temperatures to be reduced to an intermediate-temperature range, 500–700 °C [5–8]. However, at such low temperatures, the PCFC performance can be rather low due to insufficient electrochemical activity of air electrodes caused by sluggish oxygen reduction reaction (ORR) kinetics [9]. Often, the materials with predominantly electronic conductivity are used as electrodes for PCFCs, in which case the ORR is limited by a region of triple phase boundary [9,10]. From this point of view, alternative candidates with a mixed ion-electron conduction (MIEC) are more promising due to extended area of the ORR-active sites, leading to a considerable improvement of the electrodes' electrochemical activity [11–13].

Many ABO_3 perovskites are MIECs [14–17]. Prominent representatives of such MIECs are barium ferrites based on $BaFeO_3$ with no cobalt ions in their compositions. Barium, located in the A-sublattice, has a low valence state of 2+ in combination with a large ionic radius (1.61 Å at a coordination number of 12, in the Shannon system [18]), which favors the formation of a large free volume of the unit cell responsible for improved oxygen-ionic transport [9, 19]. At the same time, iron with transition valence states (Fe^{4+}/Fe^{3+}) in oxidation conditions can contribute to high catalytic activity of the electrode materials [20–22]. $BaFeO_3$ is known to adopt different crystal structures depending on the oxygen deficiency, and features of its preparation (conditions, synthesis methods, temperatures, etc.) can affect many functional properties [19, 23–25]. Therefore, doping is often used to stabilize the crystal structure and phase composition of the barium ferrite. In our study, we stabilized the crystal structure of $BaFeO_3$ *via* doping with cerium and yttrium to enhance mixed ionic-electron conductivity. Additionally, we used zirconium to improve the chemical stability of the materials. The high stability of BO_6 octahedrons provides the structural stability of ABO_3 perovskites. The acid-basic theory suggests that stronger bases bind more strongly to strong acids. Zirconium and yttrium, considered as strong acids, form the strongest metal-oxygen bonds, thus stabilizing barium ferrite-based materials effectively [26, 27]. Recently, we provided a detailed analysis on the preparation of $BaCe_{0.7-x}Fe_xZr_{0.2}Y_{0.1}O_{3-\delta}$ materials [28] as well as their application as air electrodes for PCFCs [29] and oxygen permeation membranes [30]. These works show a great promise of the designed materials in terms of their electrochemical properties. This work is directed to the investigation of the chemical stability of $BaCe_{0.7-x}Fe_xZr_{0.2}Y_{0.1}O_{3-\delta}$ materials under aggressive atmospheres, which are close to working conditions. In addition, the chemical interaction of air electrodes with a state-of-the-art proton-conducting electrolyte, $BaCe_{0.5}Zr_{0.3}Y_{0.1}Yb_{0.1}O_{3-\delta}$ (BCZYYb), was studied.

2. Experimental part

2.1. Sample preparation

The powders of $BaCe_{0.7-x}Fe_xZr_{0.2}Y_{0.1}O_{3-\delta}$ (x = 0.5, 0.6, 0.7; labeled as BCZYFx) composition were prepared by citrate-nitrate synthesis. Highly pure barium, cerium, yttrium, iron nitrates, and zirconium oxynitrate were used as starting materials. After dissolution of stoichiometric amounts of these powders in distilled water, citric acid was added as a complexing agent. The molar ratio of citric acid to total metal ions was about 1.5. The obtained homogeneous solution was gradually heated to 270 °C until complete water evaporation and the formation of a gel, which subsequently was self-ignited to form a highly dispersed powder. Synthesis of the obtained powders was carried out in two stages with intermediate homogenization: at 1050 °C (5 h) to remove organic impurities and then at 1100 °C (5 h) to complete the phase formation and crystallization. The obtained powders were uniaxially pressed into tablets (20 mm diameter and 1 mm thickness) at a pressure of 250 MPa and then sintered at 1350 °C for 5 h.

An electrolyte BCZYYb powder was also prepared by the citrate-nitrate synthesis method. Barium, cerium, yttrium, ytterbium nitrates, and zirconium oxynitrate were used as starting materials. Citric acid was used as a complexing agent and fuel in a molar ratio of 1:1 between the total amounts of metal cations and citric acid. The starting compounds were dissolved in a minimum amount of distilled water in a heat resistant beaker. For complete dissolution of the salts, the resulting mixture was heated to 150 °C and kept at this temperature for 10 min. After obtaining a homogeneous solution, it was evaporated at 270 °C until a gel-like mass was formed. A subsequent increase in temperature to 370 °C resulted in a spontaneous combustion of a residue to form a highly dispersed powder. After homogenization via an agate mortar and pestle, the electrolyte powder was subjected to a two-step synthesis with intermediate grinding at 1050 (5 h) and 1100 °C (5 h).

2.2. Chemical stability and compatibility of materials

High-temperature X-ray phase analysis was performed using a Rigaku Ultima IV diffractometer equipped with a Rigaku SHT-1500 high-temperature chamber, in Co Kα radiation at λ = 1.7889 Å, in the temperature range of 25–1000 °C.

Chemical stability of ceramic $BaCe_{0.7-x}Fe_xZr_{0.2}Y_{0.1}O_{3-\delta}$ samples was investigated in atmospheres of high (70 vol.%) humidity, carbon dioxide, and hydrogen. For this purpose, the samples were treated under specified conditions at a temperature of 1100 °C for 10 h. The phase composition thereafter was confirmed using X-ray diffraction analysis (XRD) (Rigaku D/MAX-2200VL/PC, Rigaku Corporation) in Cu Kα radiation at room temperature in the angle range of 20°–80° with a scanning step of 0.02°. The XRD data were refined by the Rietveld method using FullProf software [31].

The thermal expansion of the materials was investigated using a Netsch DIL 402C dilatometer at temperatures from 100 to 1100 °C. The thermal expansion coefficients (TECs) was then determined from linear sections of the dilatometric curves.

The surface morphology and the presence/absence of secondary phases were investigated using scanning electron microscopy (SEM, TESCAN VEGA, Tescan s.r.o.). The structure of the powders treated in different atmospheres was analyzed by Raman (Renishaw U 1000, Renishaw plc) and IR spectroscopy (Bruker Tensor 27 FT-IR Spectrometer, Bruker Corporation) analyses.

The chemical interaction between single-phase powders of BCZYFx electrode and BCZYYb electrolyte was studied by their mixing in a weight ratio of 1:1. The obtained mixtures were calcined at 1100 °C for 10 h. The presence and phase composition of chemical interaction products were investigated by XRD analysis.

3. Results and Discussion

3.1. High-temperature X-ray phase analysis

To investigate phase stability of the powder materials, XRD analysis was carried out at 50–1000 °C (HT-XRD). The HT-XRD analysis was carried out for the BCZYF0.6 sample as an example. Diffractograms obtained at room temperature before (RT) high-temperature measurements were compared with diffractograms obtained at room temperature after (RT*) high-temperature measurements. As can be seen from Figure 1, the cubic perovskite structure of BCZYF0.6 was maintained over the entire studied temperature range. The observed shift of diffractogram reflections towards smaller angles with increasing temperature indicates an increase in the unit cell parameters, which is primarily due to thermal expansion. The temperature dependences of the unit cell relative linear change in the unit cell parameter *a* (Figure 2) were calculated from the HT-XRD results.

Previously, we published a study presenting the thermal behavior of materials based on barium cerate-zirconates doped with iron in a wide range of its concentrations [25]. It was found that the samples with a relatively high iron concentration have an inflection point at a temperature of around 550 °C, which indicates a change in TECs values. We hypothesize that this deviation is linked to the occurrence of chemical expansion, which accompanies the thermal expansion. This could be attributable to the reduction of lattice iron from Fe^{4+} to Fe^{3+}. As a result, there is an increase in the ionic radius of the iron: $r_{\mathrm{Fe}^{4+}} = 0.585$ Å, $r_{\mathrm{Fe}^{3+}_{\mathrm{LS}}} = 0.55$ Å, $r_{\mathrm{Fe}^{3+}_{\mathrm{HS}}} = 0.645$ Å. The HT-XRD and dilatometry data for BCZYF0.6 were correlated with each other to compare the expansion behavior in static and dynamic conditions (Figure 3). In the low temperature range up to 500–550 °C, the slope of both curves was found to be similar, indicating the closeness of the TECs values obtained via HT-XRD and dilatometry ($12.1\cdot10^{-6}$ and $14.2\cdot10^{-6}$ K^{-1}, respectively). However, as the temperature increases, the TECs values obtained by HT-XRD ($7.4\cdot10^{-6}$ K^{-1}) show a decrease compared to $16.8\cdot10^{-6}$ K^{-1} obtained by dilatometry. The observed discrepancy can be attributed to different measurement modes: isothermal one for HT-XRD analysis and dynamic one for dilatometry.

Summarizing all of the above, we can conclude that thermal expansion is coupled with chemical expansion in the studied samples. The latter is due to the loss of lattice oxygen and partial reduction of iron cations with increasing temperature.

3.2. Chemical compatibility with electrolytes

The investigation of chemical interaction with the widely used electrolyte material based on cerate-zirconates was carried out at three temperatures: 1200, 1250, and 1350 °C. The temperatures were selected in order to investigate the chemical interaction between the electrodes and electrolyte in high-temperature conditions. The calcined mixtures of BCZYFx (*x* = 0.5, 0.6, 0.7) electrode powders and BCZYYb electrolyte were analyzed using the XRD (Figures 4–6).

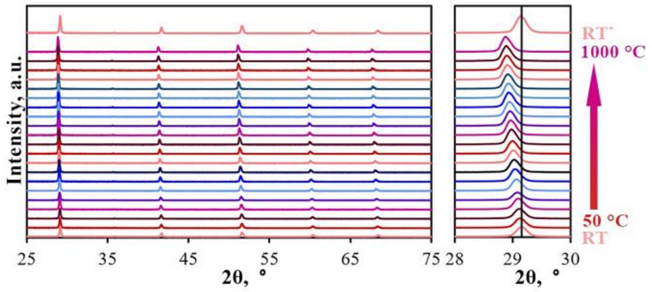

Figure 1 High-temperature XRD data for the $BaCe_{0.1}Fe_{0.6}Zr_{0.2}Y_{0.1}O_{3-\delta}$ material between 50 and 1000 °C with a step of 50 °C in wide (b) and narrow (b) range of angles.

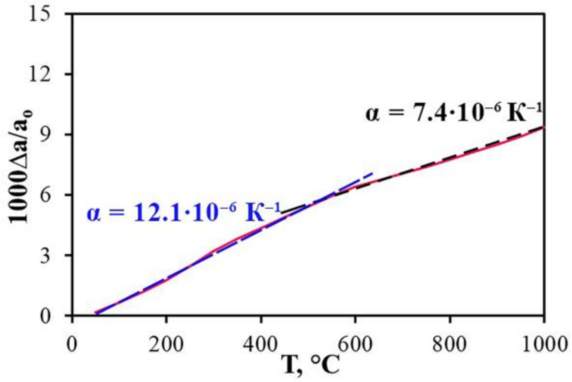

Figure 2 Temperature dependence of the relative change of the unit cell parameter for the $BaCe_{0.1}Fe_{0.6}Zr_{0.2}Y_{0.1}O_{3-\delta}$ sample and calculated values of TECs.

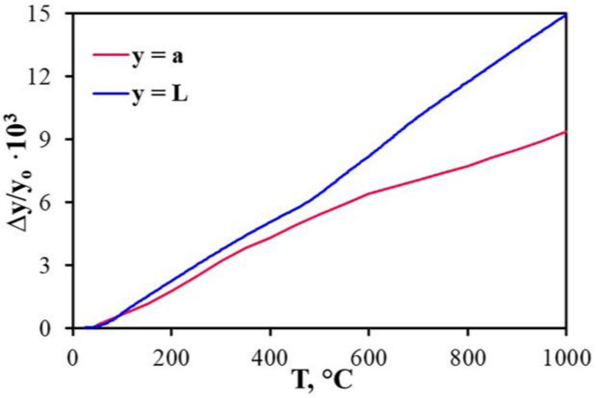

Figure 3 Temperature dependences of the relative change of the unit cell parameter and linear dimensions for the $BaCe_{0.1}Fe_{0.6}Zr_{0.2}Y_{0.1}O_{3-\delta}$ sample.

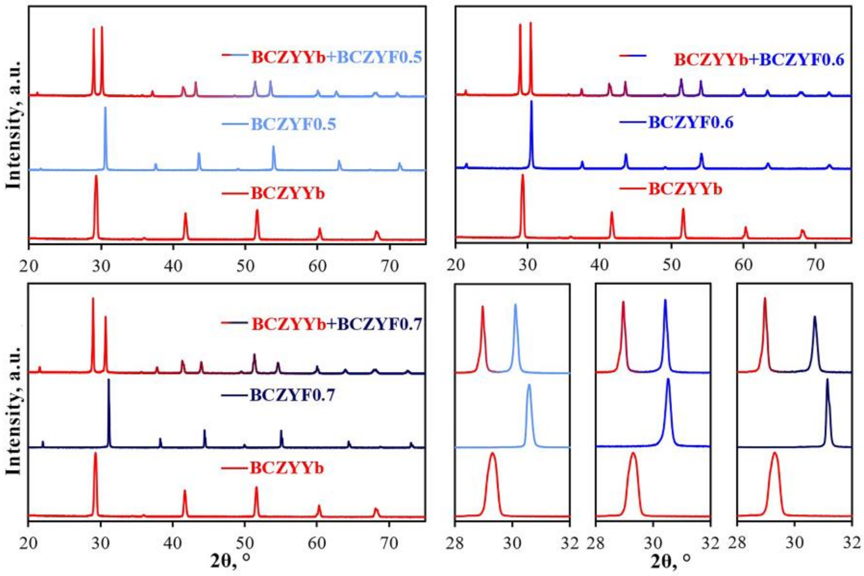

Figure 4 XRD patterns of $BaCe_{0.5}Zr_{0.3}Y_{0.1}Yb_{0.1}O_{3-\delta}$ and $BaCe_{0.7-x}Fe_xZr_{0.2}Y_{0.1}O_{3-\delta}$ compositions after their co-firing at 1200 °C for 10 h.

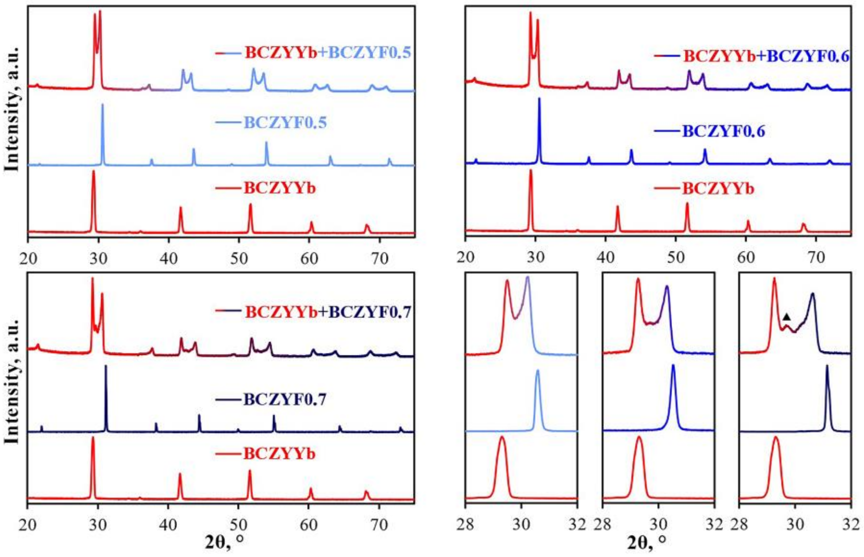

Figure 5 XRD patterns of $BaCe_{0.5}Zr_{0.3}Y_{0.1}Yb_{0.1}O_{3-\delta}$ and $BaCe_{0.7-x}Fe_xZr_{0.2}Y_{0.1}O_{3-\delta}$ compositions after their co-firing at 1250 °C for 10 h, marker indicates impurity phase based on barium zirconate.

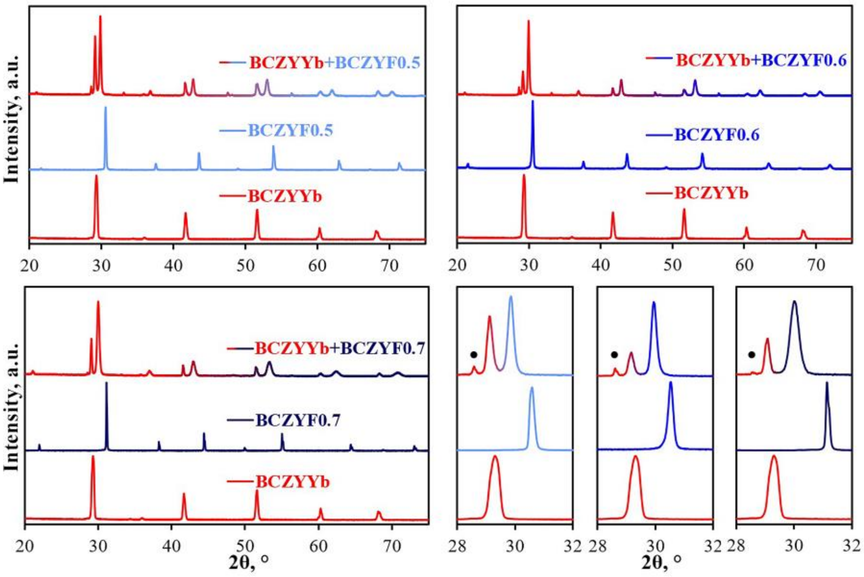

Figure 6 XRD patterns of $BaCe_{0.5}Zr_{0.3}Y_{0.1}Yb_{0.1}O_{3-\delta}$ and $BaCe_{0.7-x}Fe_xZr_{0.2}Y_{0.1}O_{3-\delta}$ compositions after their co-firing at 1350 °C for 10 h, marker indicates impurity phase based on cerium dioxide.

DOI: 10.15826/chimtech.2023.10.4.14

The initial powder of BCZYYb electrolyte had a rhombohedral structure with space group of R$\overline{3}$c, while the electrodes exhibited a cubic perovskite structure with Pm$\overline{3}$m space group.

It was found that after exposure at 1200 °C, no additional extra reflections were observed in the XRD patterns, indicating the absence of impurity phases (Figure 4). According to the Rietveld refinement procedure (the results are presented in Table S1), the identified peaks in the XRD pattern correspond to the space groups of the initial electrolyte and electrode materials. As can be seen from Figure 5, after a long exposure at 1250 °C, an additional peak is observed between the main phase reflections, corresponding to the formation of a secondary phase identified as barium zirconate. The stronger chemical interaction occurs at the higher concentration of iron. Obviously, the unit cell volume of the formed phase with space group Pm$\overline{3}$m (Table S2) is larger than the unit cell volume of iron-doped barium zirate-zirconate with the same space group. The smaller iron ionic radii of $r_{\mathrm{Fe}^{4+}} = 0.585$ Å, $r_{\mathrm{Fe}^{3+}_{\mathrm{HS}}} = 0.645$ Å indicate that the obtained phase is iron deficient due to a size factor. This is in contrast to the larger ionic radii of the matrix cations on the B-sublattice, such as $r_{\mathrm{Ce}^{4+}} = 0.87$ Å, $r_{\mathrm{Zr}^{4+}} = 0.72$ Å, $r_{\mathrm{Y}^{3+}} = 0.90$ Å [18].

A further increase of temperature up to 1350 °C (see Figure 6) results in the emergence of an impurity phase identified as cerium dioxide with space group Fm$\overline{3}$m. The refinement results indicate that the amount of CeO_2 impurity phase does not exceed 4% (Table S3). The phase identified as barium ferrite retains its cubic structure, in contrast to the electrolyte phase, which acquires the orthorhombic structure with the space group Imma.

Raising the temperature exacerbates the chemical interaction between BCZYFx electrodes (where x = 0.5, 0.6, 0.7) and BCZYYb electrolyte. Nevertheless, the indicated temperatures are much higher than the firing temperature of the investigated electrodes and operating temperatures of PCFCs. Consequently, the absence of strong chemical interaction between the two materials at 1200 °C allows us to conclude about the relatively good stability of these phases.

3.3. Materials chemical stability in different atmospheres

Aggressive media can cause electrode poisoning by forming weakly conducting compounds, such as hydroxides, carbonates, and simple oxides. The formation of impurity phases can significantly affect the electrochemical properties of the electrode materials. The deterioration of electrochemical activity can result from the formation of a secondary phase based on barium carbonate. Furthermore, inadequate mixed ionic-electronic conductivity of the generated phases can restrict ORR solely to the three-phase boundary, resulting in the deterioration of its kinetics as well.

$BaCe_{0.7-x}Fe_xZr_{0.2}Y_{0.1}O_{3-\delta}$ were investigated in atmospheres of high (70%) humidity, carbon dioxide and hydrogen. For this purpose, the samples were exposed under the specified conditions at 1100 °C for 10 h. The phase composition was determined through XRD analysis, see Figure 7.

Treatments in a high humidity environment (Figure 7a) resulted in the appearance of a secondary phase based on barium zirconate only in the BCZYF0.6 sample. The remaining samples retained their single-phase state. The XRD patterns of the samples subjected to a carbon dioxide atmosphere (represented in Figure 7b) indicate that no interactions between the ceramic samples and the gas components were observed. The phase composition was significantly changed after the treatments of the studied materials in a hydrogen atmosphere, as illustrated in Figure 7c. The XRD patterns of all three ceramic samples show additional peaks consistent with the presence of a reduced metallic iron phase. It is seen that the atmosphere has a greater influence on the phase composition of the materials with lower iron content. Therefore, the same phase reflections are observed to shift to smaller angles in addition to the reflections of the main phase of barium ferrite seen in the XRD spectra of BCZYF0.5. These observations may indicate the existence of a separate phase with a large unit cell volume, such as a phase based on $BaCe_{0.7-x}Fe_xZr_{0.2}Y_{0.1}O_{3-\delta}$ that is iron-deficient. This phenomenon can be attributed to the ionic radii of the dopants.

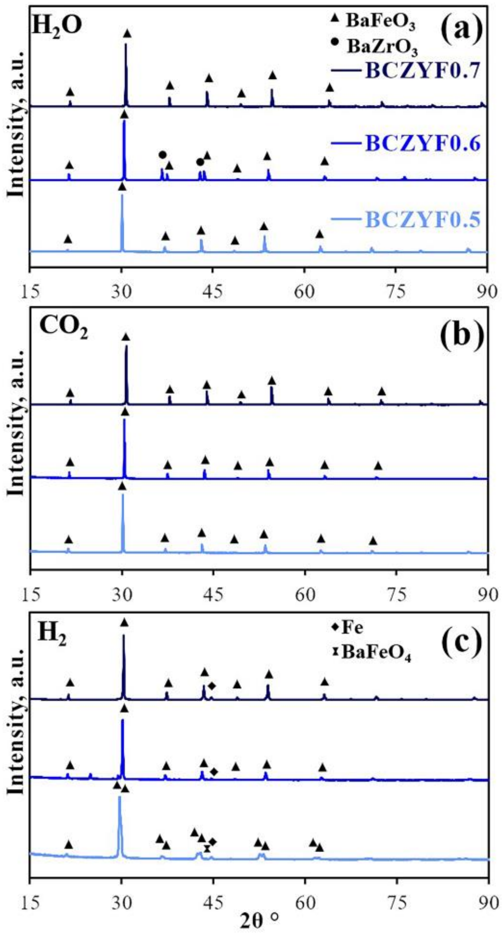

Figure 7 XRD patterns of the $BaCe_{0.7-x}Fe_xZr_{0.2}Y_{0.1}O_{3-\delta}$ samples after their treatments in high (70%) humidity, carbon dioxide, and hydrogen atmospheres at 1100 °C for 10 h.

DOI: 10.15826/chimtech.2023.10.4.14

As it was indicated earlier, due to the significantly larger ionic radius of cerium compared to iron, the expansion of the unit cell volume in the secondary phase of the complex oxide can be attributed to the decrease in iron concentration and the increase in cerium concentration. The XRD findings for the BCZYF0.6 sample demonstrate a peak linked to minimal amounts of cerium and zirconium oxides, as well as reflections related to metallic iron. The samples with x = 0.6 and 0.7 display acceptable stability in operating environments. This aspect is advantageous, as these materials can be employed as PCFC oxygen and fuel electrodes.

The SEM analysis was performed for the ceramic samples exposed to various atmospheres, as shown in Figure 8. These results show the formation of tiny main phase crystals on the sample surface. The conclusions drawn from the XRD analysis are supported by the SEM images for the samples exposed to high humidity. The microphotograph of the sample BCZYF0.6 shows crystal flakes of the primary phase along with significantly lighter particles on the surface of grains, indicating the existence of the secondary phase of barium zirconate. The micrographs of the samples after exposure to hydrogen demonstrate that reduced iron was formed on the surface of the grains. These findings are also confirmed by XRD results. At the same time, as the concentration of Fe dopant in the composition increases, there is an increase in the number and size of reduced iron particles, which is also supported by the XRD results.

Figure 9 presents the examples of IR spectra for the BCZYF0.5 and BCZYF0.7 compositions. These spectra were recorded at room temperature, covering a wave number range from 400 to 3800 cm⁻¹. The powders studied were exposed to atmospheres of H_2O, H_2, and CO_2 for extended periods. The prominent absorption peaks observed at 590 cm⁻¹ are associated with the stretching vibrations of Fe–O bonds within BO_6 octahedra [32–35]. The Fe–O–Fe groups displaying metal-oxygen-metal bonding are represented by peaks found at wave numbers of 1120–1130 cm⁻¹ [36]. The peaks associated with the symmetric stretching vibrations of the carboxyl group can be identified at wave numbers of 2360–2370 cm⁻¹. [37]. The asymmetric vibration peaks of the same group are located at 1420 [36, 37] and 1630 cm⁻¹ [36]. The peaks between 3465 and 3485 cm⁻¹ [36] suggest the occurrence of stretching and strain vibrations of the hydroxyl group (H–O–H) absorbed from an atmosphere. It is important to note that IR spectroscopy method does not have the capability of identifying the existence of secondary phases, which does not contradict the XRD results. Furthermore, in the samples where x = 0.7, the frequencies of oscillation and widths of absorption bands are greater (in comparison to the sample where x = 0.5) irrespective of the gas compositions.

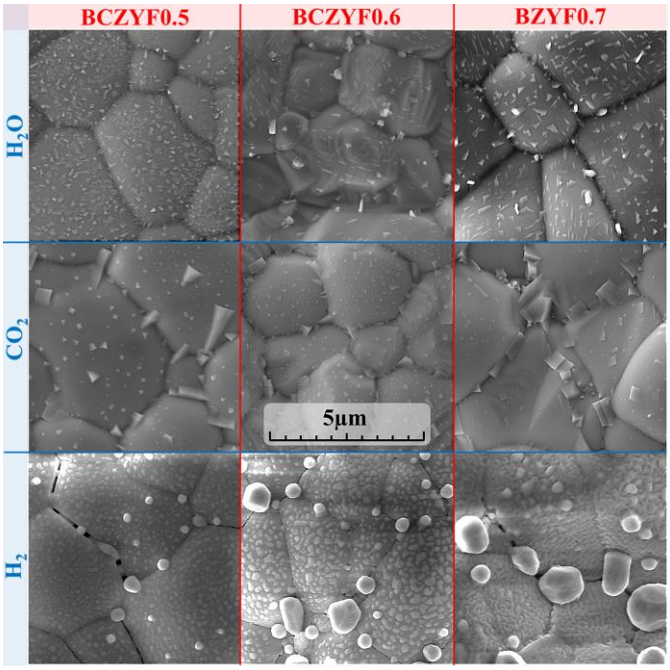

Figure 8 SEM images of $BaCe_{0.7-x}Fe_xZr_{0.2}Y_{0.1}O_{3-\delta}$ samples after their treatments in high (70%) humidity, carbon dioxide, and hydrogen atmospheres at 1100 °C for 10 h.

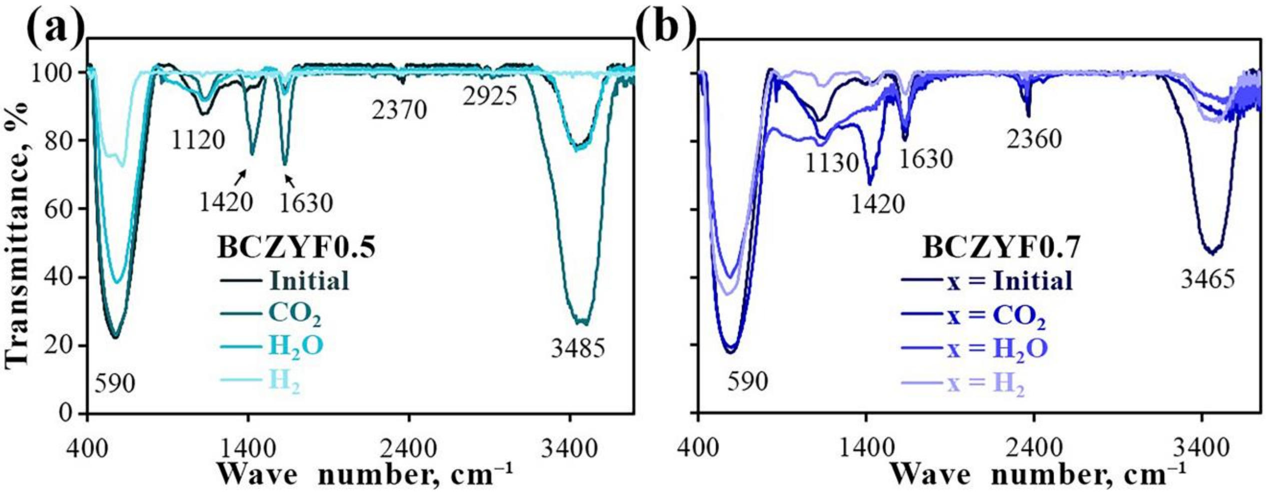

Figure 9 IR spectra of the samples with BCZYF0.5 (a) and BCZYF0.7 (b) compositions after their treatments in different atmospheres at 1100 °C for 10 h.

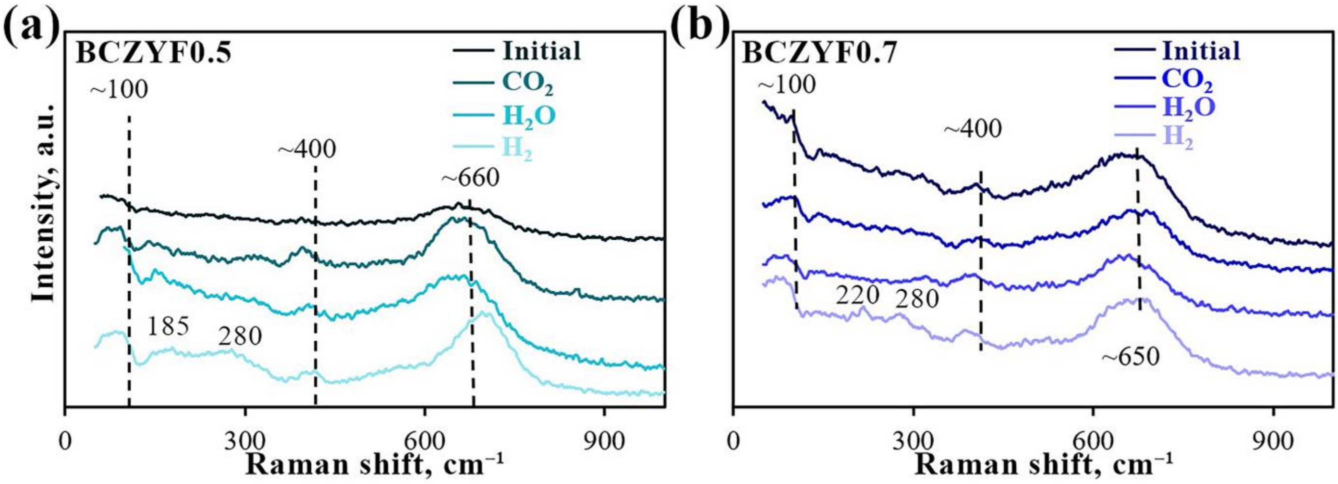

Figure 10 Raman spectra of the samples with BCZYF0.5 (a) and BCZYF0.7 (b) compositions after their treatments in different atmospheres at 1100 °C for 10 h.

Raman spectroscopy was employed to map the lattice vibrations, crystal structure, and detect impurity phases. The Raman spectra for BCZYF0.5 and BCZYF0.7 are shown in Figures 10a and 10b, respectively. In the crystal structure of a comparable cubic barium zirconate, the Ba atom is located at the corner of the cube, the Zr atom at the centre of the body and the O atom at the centre of the face. The Zr atom, in this case, creates an octahedral ZrO_6 cluster, while the Ba atom creates a cubo-octahedral BaO_{12} cluster [38]. It is assumed that in the case of an ideal cubic perovskite (ABO_3), no first-order active modes would be observable in the Raman spectra since the phonons of its zone centre are in a centrosymmetric position [39, 40]. However, according to the literature reports active first-order Raman modes can be detected for real cubic perovskites when their centrosymmetry is violated or distorted by defects caused by acceptor doping, deformations, or impurities [38, 41].

The interpretation of the Raman spectroscopy data is based on the previous studies and literature sources, although the approaches are different. Asymmetric modes of BO_6 octahedra are associated with Raman scattering (Figure 10) at 100 cm⁻¹ for the first-order modes and at 400 cm⁻¹ for the second-order modes. The vibrations of locally distorted ZrO_6 octahedra are attributed to the modes found in the range of 650–660 cm⁻¹ [42]. Raman spectra collected within the range of 50–1000 cm⁻¹ indicate that the original structure was not destroyed for both samples of BCZYF0.5 and BCZYF0.7.

4. Limitations

This study's limitation lies in the challenge of interpreting SEM findings, specifically in determining the composition of the separated phases on ceramic surfaces. Although the XRD analysis successfully identified the primary phases, linking this data to the SEM results with complete certainty is challenging.

Investigations were conducted into chemical stability of the materials in aggressive atmospheric conditions following 10 h of such an exposure at 1100 °C. This study utilizes the XRD, SEM, IR and Raman spectroscopy methods at room temperatures; this approach limits the ability to directly consider the processes of interaction of materials with high-temperature gas mixtures.

5. Conclusions

The chemical stability of the materials based on $BaCe_{0.7-x}Fe_xZr_{0.2}Y_{0.1}O_{3-\delta}$ (BCZYFx) was investigated in this work. Firstly, the thermal behavior of the BCZYF0.6 complex oxide was studied by HT-XRD. The material being studied has no phase transitions and undergoes an increase in unit cell volume due to thermal expansion. The interaction between the electrodes and proton-conducting electrolytes based on $BaCe_{0.5}Zr_{0.3}Y_{0.1}Yb_{0.1}O_{3-\delta}$ after long-term (10 h) co-firing at 1200, 1250 and 1350 °C was investigated. The XRD results showed no chemical reaction between BCZYFx (x = 0.5, 0.6, 0.7) and BCZYYb at 1200 °C. However, there is a progressive interaction between these materials at higher co-firing temperatures. Nevertheless, all the temperatures studied are significantly higher than the calcination and operating temperatures of PCFCs, which allows us to predict the relatively good stability of the electrode and electrolyte phases. The chemical stability studies also concerned the stability of the materials in aggressive atmospheres: high (70 vol.%) humidity, carbon dioxide and hydrogen. Thus, from the XRD results it can be concluded that the samples with x = 0.6 and 0.7 are characterized by acceptable stability under such atmospheres. The XRD results were confirmed by the SEM analysis. The results of IR spectroscopy showed no significant changes in the structure of the materials after their treatments in all atmospheres except hydrogen. Under these testing conditions, it was observed that BCZYF0.5 was the stablest sample, in contrast to BCZYF0.7. However, as this method does not enable the identification of secondary phases, the results cannot contradict the XRD information.

DOI: 10.15826/chimtech.2023.10.4.14

The Raman spectroscopic results indicate that there was no destruction of the initial structure in both BCZYF0.5 and BCZYF0.7 samples. It can be concluded that the developed electrode materials possess satisfactory chemical stability in atmospheres containing high (70%) humidity, carbon dioxide, and hydrogen, since all the studies were carried out at deliberately increased temperatures and the detected evidence of chemical transformations is insignificant.

• Supplementary materials

This manuscript contains supplementary materials, which are available on the corresponding online page.

• Funding

This work was financially supported by the President of the Russian Federation's scholarship to junior scientists and postgraduate students, no. СП-210.2022.1, https://grants.ex-tech.ru.

• Acknowledgments

The authors acknowledge St. Petersburg State University and the Centre for XRD Studies. Characterizations of powder and ceramic materials were carried out at the Shared Access Centre "Composition of Compounds" of Institute of High-Temperature Electrochemistry.

• Author contributions

Conceptualization: L.T.
Methodology: L.T., G.V.
Software: L.T., G.V.
Validation: L.T.
Formal analysis: S.P., E.V., A.M.
Investigation: L.T., S.P., E.V.
Data curation: L.T. S.P., E.V.
Writing—original draft preparation: L.T.
Writing—review and editing: L.T.
Visualization: S.P., E.V., L.T.
Supervision: L.T.
Project administration: L.T.
Funding acquisition: L.T.

• Conflict of interest

The authors declare no conflict of interest.

• Additional information

Author IDs:

Liana Tarutina, Scopus ID 57208683245;
Inna Starostina, Scopus ID 58655593700;
Gennady Vdovin, Scopus ID 35569602600;
Svetlana Pershina, Scopus ID 56281284300;
Emma Vovkotrub, Scopus ID 6602135202;
Anna Murashkina, Scopus ID 8364365100.

Websites:

Institute of High-Temperature Electrochemistry, https://ihte.ru/?page_id=3106;
Ural Federal University, https://urfu.ru/en/;
Saint Petersburg State University, https://english.spbu.ru/.

References

1. Zainon AN, Somalu MR, Kamarul Bahrain AM, Muchtar A, Baharuddin NA, et al. Challenges in using perovskite-based anode materials for solid oxide fuel cells with various fuels: a review. Int J Hydrogen Energy. 2023;48:20441–20464. doi:10.1016/j.ijhydene.2022.12.192
2. Su H, Hu YH. Progress in low-temperature solid oxide fuel cells with hydrocarbon fuels. Chem Eng J. 2020;402:126235. doi:10.1016/j.cej.2020.126235
3. Liu Y, Shao Z, Mori T, Jiang SP. Development of nickel-based cermet anode materials in solid oxide fuel cells – Now and future. Mater Rep Energy. 2021;1:100003. doi:10.1016/j.matre.2020.11.002
4. Singh M, Zappa D, Comini E. Solid oxide fuel cell: Decade of progress, future perspectives and challenges. Int J Hydrogen Energy. 2021;46:27643–74. doi:10.1016/j.ijhydene.2021.06.020
5. Hossain MK, Chanda R, El-Denglawey A, Emrose T, Rahman MT, Biswas MC, et al. Recent progress in barium zirconate proton conductors for electrochemical hydrogen device applications: A review. Ceram Int. 2021;47:23725–23748. doi:10.1016/j.ceramint.2021.05.167
6. Nur Syafkeena MA, Zainor ML, Hassan OH, Baharuddin NA, Othman MHD, Tseng C-J, et al. Review on the preparation of electrolyte thin films based on cerate-zirconate oxides for electrochemical analysis of anode-supported proton ceramic fuel cells. J Alloys Compd. 2022;918:165434. doi:10.1016/j.jallcom.2022.165434
7. Kasyanova AV, Zvonareva IA, Tarasova NA, Bi L, Medvedev DA, Shao Z. Electrolyte materials for protonic ceramic electrochemical cells: Main limitations and potential solutions. Mater Rep Energy. 2022:100158. doi:10.1016/j.matre.2022.100158
8. Zvonareva IA, Medvedev DA. Proton-conducting barium stannate for high-temperature purposes: A brief review. J Eur Ceram Soc. 2023;43:198–207. doi:10.1016/j.jeurceramsoc.2022.10.049
9. Wei Z, Wang J, Yu X, Li Z, Zhao Y, Chai J. Study on Ce and Y co-doped $BaFeO_{3-\delta}$ cubic perovskite as free-cobalt cathode for proton-conducting solid oxide fuel cells. Int J Hydrogen Energy. 2021;46:23868–23878. doi:10.1016/j.ijhydene.2021.04.188
10. Tarutin AP, Filonova EA, Ricote S, Medvedev DA, Shao Z. Chemical design of oxygen electrodes for solid oxide electrochemical cells: A guide. Sustain Energy Technol Ass. 2023;57:103185. doi:10.1016/j.seta.2023.103185
11. Yang L, Ren X, Peng W, Wang A, Yan D, Li J, et al. Triple-conducting Zn-doped $Pr_{1.8}Ba_{0.2}NiO_{4+\delta}$ air electrodes for proton ceramic electrolysis cells. J Power Sources. 2023;586:233652. doi:10.1016/j.jpowsour.2023.233652
12. Chen L, Jing J, Lun P, Zhang P, Zheng Z, Wang H, et al. $Ba_{0.9}Co_{0.7}Fe_{0.2}Nb_{0.1}O_{3-\delta}$ perovskite as promising cathode material for proton ceramic fuel cell. Int J Hydrogen Energy. 2023. doi:10.1016/j.ijhydene.2023.07.041
13. Pei Y, Wang H, Gong J, Yan Z, Xu L, Liu X, et al. Co and Hf co-doped $BaFeO_3$ cathode with obviously enhanced catalytic activity and CO_2 tolerance for solid oxide fuel cell. Int J Hydrogen Energy. 2022;47:37945–37955. doi:10.1016/j.ijhydene.2022.08.283

14. Liu H, Zhu K, Liu Y, Li W, Cai L, Zhu X, et al. Structure and electrochemical properties of cobalt-free perovskite cathode materials for intermediate-temperature solid oxide fuel cells. Electrochim Acta. 2018;279:224–230. doi:10.1016/j.electacta.2018.05.086
15. Wang M, Su C, Zhu Z, Wang H, Ge L. Composite cathodes for protonic ceramic fuel cells: Rationales and materials. Composites Part B Eng. 2022;238:109881. doi:10.1016/j.compositesb.2022.109881
16. Hanif MB, Rauf S, Abadeen Z ul, Khan K, Tayyab Z, Qayyum S, et al. Proton-conducting solid oxide electrolysis cells: Relationship of composition-structure-property, their challenges, and prospects. Matter. 2023;6:1782–1830. doi:10.1016/j.matt.2023.04.013
17. Yang Q, Lu J, Li C, Tian D, Ding Y, Lu X, et al. Tailoring the electrochemical reduction kinetics of dual-phase $BaCe_{0.5}Fe_{0.5}O$ cathode via incorporating Mo for IT-SOFCs. J Eur Ceram Soc. 2023;43:6180–6188. doi:10.1016/j.jeurceramsoc.2023.06.006
18. Shannon RD. Revised effective ionic radii and systematic studies of interatomic distances in halides and chalcogenides. Acta Cryst A. 1976;32:751–767. doi:10.1107/S0567739476001551
19. Dong F, Ni M, He W, Chen Y, Yang G, Chen D, et al. An efficient electrocatalyst as cathode material for solid oxide fuel cells: $BaFe_{0.95}SnO_{3-\delta}$. J Power Sources. 2016;326:459–465. doi:10.1016/j.jpowsour.2016.07.023
20. Wang J, Lam KY, Saccoccio M, Gao Y, Chen D, Ciucci F. Ca and In co-doped $BaFeO_{3-\delta}$ as a cobalt-free cathode material for intermediate-temperature solid oxide fuel cells. J Power Sources. 2016;324:224–232. doi:10.1016/j.jpowsour.2016.05.089
21. Cui J, Wang J, Zhang X, Li G, Wu K, Cheng Y, et al. Low thermal expansion material $Bi_{0.5}Ba_{0,5}FeO_{3-\delta}$ δ in application for proton-conducting ceramic fuel cells cathode. Int J Hydrogen Energy. 2019;44:21127–21135. doi:10.1016/j.ijhydene.2019.02.127
22. Raimondi G, Merkle R, Longo A, Giannici F, Mathon O, Sahle CJ, et al. Interplay of chemical, electronic, and structural effects in the triple-conducting $BaFeO_3$ –Ba(Zr,Y)O_3 solid solution. Chem Mater. 2023;35: 8945–8957. doi:10.1021/acs.chemmater.3c01538
23. Zhu X, Wang H, Yang W. Structural stability and oxygen permeability of cerium lightly doped $BaFeO_{3-\delta}$ ceramic membranes. Solid State Ionics. 2006;177:2917–2921. doi:10.1016/j.ssi.2006.08.027
24. He W, Fan J, Zhang H, Chen M, Sun Z, Ni M. Zr doped $BaFeO_{3-\delta}$ as a robust electrode for symmetrical solid oxide fuel cells. Int J Hydrogen Energy. 2019;44:32164–32169. doi:10.1016/j.ijhydene.2019.10.091
25. Akbari-Fakhrabadi A, Fábrega G, Ochoa P, Meruane V, Valenzuela P, Gacitúa W. Effect of La^{3+} and Nb^{5+}on structural and mechanical properties of $BaFeO3_{3-\delta}$. J Eur Ceram Soc. 2023;43:6162–6169. doi:10.1016/j.jeurceramsoc.2023.05.017
26. Wang Z, Wang Y, Wang J, Song Y, Robson MJ, Seong A, et al. Rational design of perovskite ferrites as high-performance proton-conducting fuel cell cathodes. Nat Catal. 2022;5:777–787. doi:10.1038/s41929-022-00829-9
27. Hu H, Lu Y, Zhou X, Li J, Wang X, Ding X. A/B-site co-doping enabled fast oxygen reduction reaction and promoted CO_2 tolerance of perovskite cathode for solid oxide fuel cells. J Power Sources. 2022;548:232049. doi:10.1016/j.jpowsour.2022.232049
28. Tarutina LR, Vdovin GK, Lyagaeva JG, Medvedev DA. $BaCe_{0.7-x}Zr_{0.2}Y_{0.1}Fe_xO_{3-\delta}$ derived from proton-conducting electrolytes: A way of designing chemically compatible cathodes for solid oxide fuel cells. J Alloys Compd. 2020;831:154895. doi:10.1016/j.jallcom.2020.154895
29. Tarutina LR, Kasyanova AV, Starostin GN, Vdovin GK, Medvedev DA. Electrochemical activity of original and infiltrated Fe-doped Ba(Ce,Zr,Y)O_3-based electrodes to be used for protonic ceramic fuel cells. Catalysts. 2022;12:1421. doi:10.3390/catal12111421
30. Tarutina LR, Vdovin GK, Lyagaeva JG, Medvedev DA. Comprehensive analysis of oxygen transport properties of a $BaFe_{0.7}Zr_{0.2}Y_{0.1}O_{3-\delta}$-based mixed ionic-electronic conductor. J Membr Sci. 2021;624:119125. doi:10.1016/j.memsci.2021.119125
31. FullProf Suite. Crystallographic tools for Rietveld, profile matching & integrated intensity refinements of X-Ray and/or neutron data [Internet]. https://www.ill.eu/sites/fullprof/, Accessed on 15 September 2023.
32. Shen P, Luo J, Zuo Y, Yan Z, Zhang K. Effect of La-Ni substitution on structural, magnetic and microwave absorption properties of barium ferrite. Ceram Int. 2017;43:4846–4851. doi:10.1016/j.ceramint.2016.12.107
33. Patel CD, Dhruv PN, Meena SS, Singh C, Kavita S, Ellouze M, et al. Influence of Co^{4+}–Ca^{2+} substitution on structural, microstructure, magnetic, electrical and impedance characteristics of M-type barium–strontium hexagonal ferrites. Ceram Int. 2020;46:24816–24830. doi:10.1016/j.ceramint.2020.05.326
34. Xian H, Zhang X, Li X, Zou H, Meng M, Zou Z, et al. Effect of the calcination conditions on the NO_x storage behavior of the perovskite $BaFeO_{3-x}$ catalysts. Catal Today. 2010;158:215–219. doi:10.1016/j.cattod.2010.03.026
35. Zhao WY, Wei P, Wu XY, Wang W, Zhang QJ. Lattice vibration characterization and magnetic properties of M-type barium hexaferrite with excessive iron. J Appl Phys. 2008;103. doi:10.1063/1.2884533
36. Shen P, Luo J, Zuo Y, Yan Z, Zhang K. Effect of La-Ni substitution on structural, magnetic and microwave absorption properties of barium ferrite. Ceram Int. 2017;43:4846–4851. doi:10.1016/j.ceramint.2016.12.107
37. Ahmad N, Alam M, Adil SF, Ansari AA, Assal ME, Ramay SM, et al. Synthesis, characterization, and selective benzyl alcohol aerobic oxidation over Ni-loaded $BaFeO_3$ mesoporous catalyst. J King Saud Univ Sci. 2020;32:2059–2068. doi:10.1016/j.jksus.2020.02.015
38. Thomas J, Anitha PK, Thomas T, Thomas N. $BaZrO_3$ based non enzymatic single component single step ceramic electrochemical sensor for the picomolar detection of dopamine. Ceram Int. 2022;48:7168–7182. doi:10.1016/j.ceramint.2021.11.278
39. Aarthi U, Babu KS. Grain boundary space charge modulation in $BaZr_{0.8}Y_{0.2-x}M_xO_{3-\delta}$ with transition metal (M= Ni, Co, Fe, and Zn) co-doping. Int J Hydrogen Energy. 2020;45:29356–29366. doi:10.1016/j.ijhydene.2020.07.207
40. Charoonsuk T, Vittayakorn N. Soft-mechanochemical synthesis of monodispersed $BaZrO_3$ sub-microspheres: Phase formation and growth mechanism. Mater Design. 2017;118:44–52. doi:10.1016/j.matdes.2017.01.029
41. Fassbender RU, de Carvalho Teixeira V, Galante D, Ferrer M, Jardim PLG, Ratmann CR, et al. Correlation between local structure and electronic properties of $BaZrO_3$:TbYb Optical Ceramics. J Electron Spectrosc Relat Phenomena. 2021;251:147106. doi:10.1016/j.elspec.2021.147106
42. Triviño-Peláez Á, Mosa J, Pérez-Coll D, Aparicio M, Mather GC. Low-temperature sintering and enhanced stability of fluorine-modified $BaZr_{0.8}Y_{0.2}O_{3-\delta}$ synthesised by a sol-gel alkoxide route. J Eur Ceram Soc. 2023;43:99–108. doi:10.1016/j.jeurceramsoc.2022.09.042